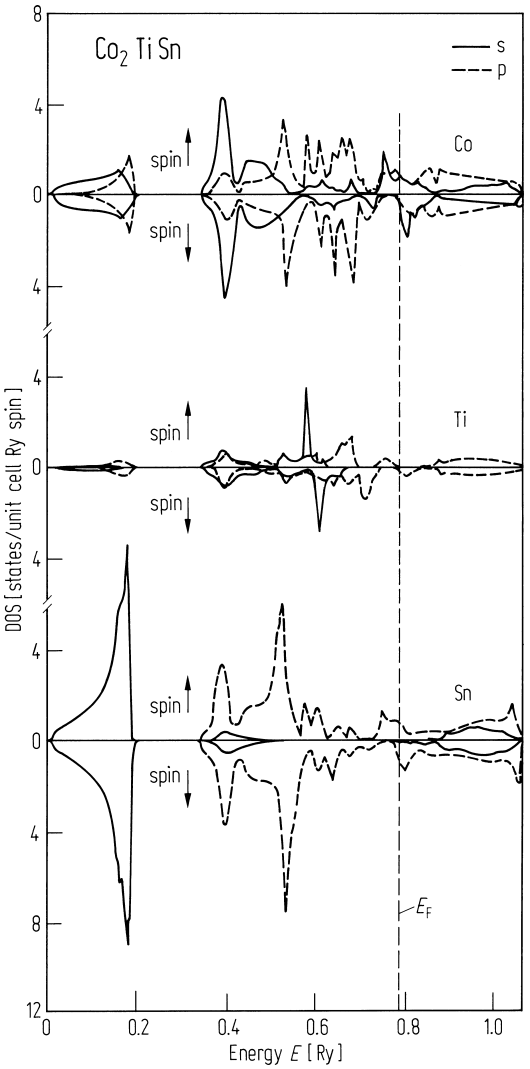

Fig. 441. DOS curves of the s and p states of Co, Ti and Sn in Co_2TiSn calculated using the LSD method [84I2].

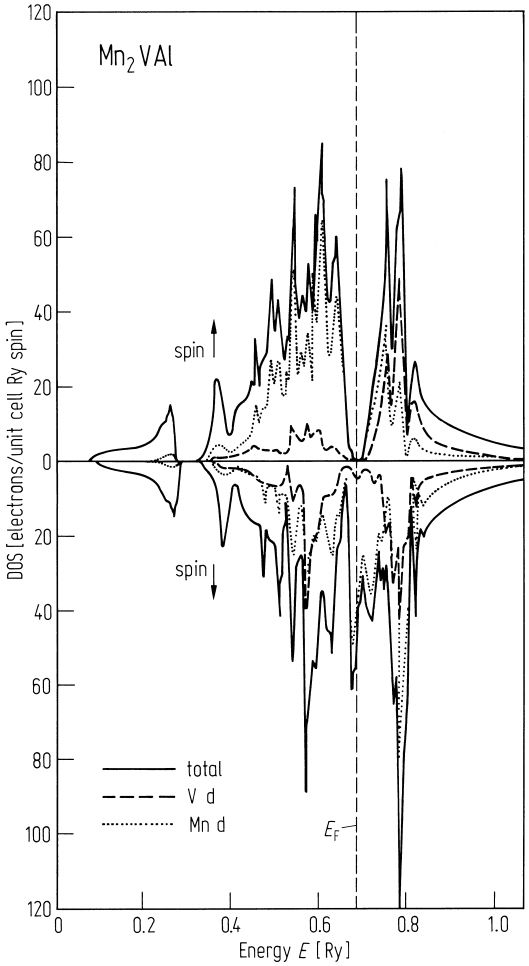

Fig. 444. DOS curves of Mn_2VAl calculated using the LSD method [84I2].

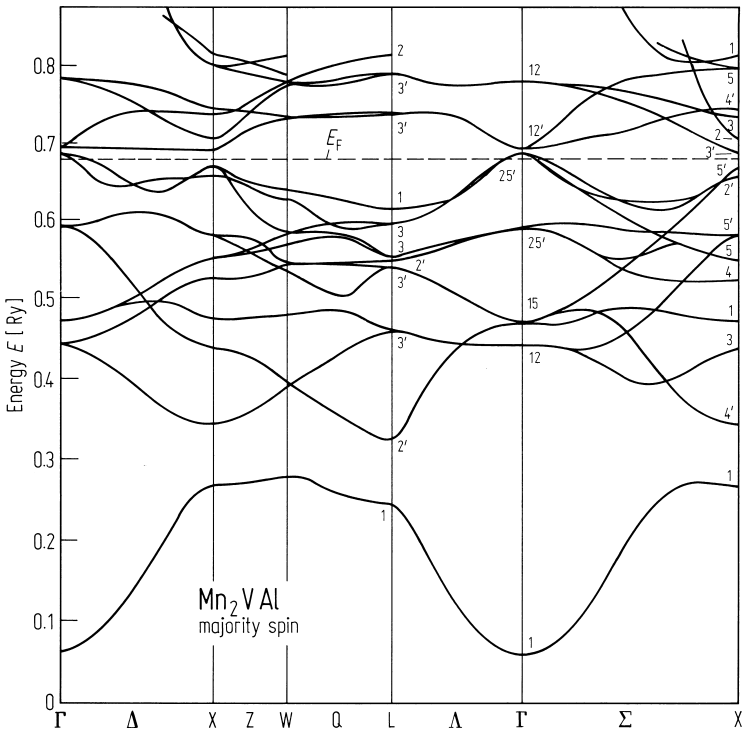

Fig. 442. $E(\boldsymbol{k})$ curves of Mn_2VAl for the majority spin state calculated using the LSD method [84I2].

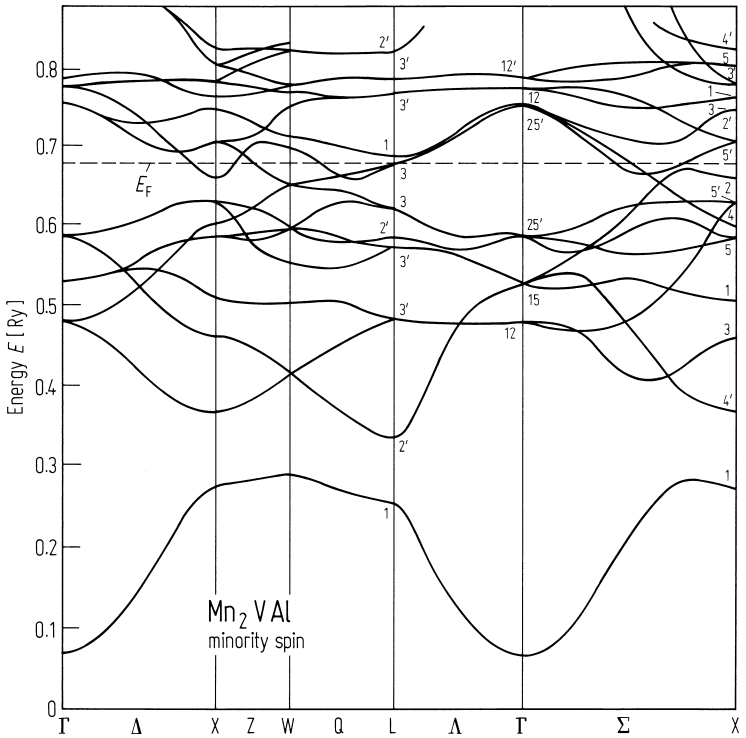

Fig. 443. $E(\boldsymbol{k})$ curves of Mn_2VAl for the minority spin state calculated using the LSD method [84I2].

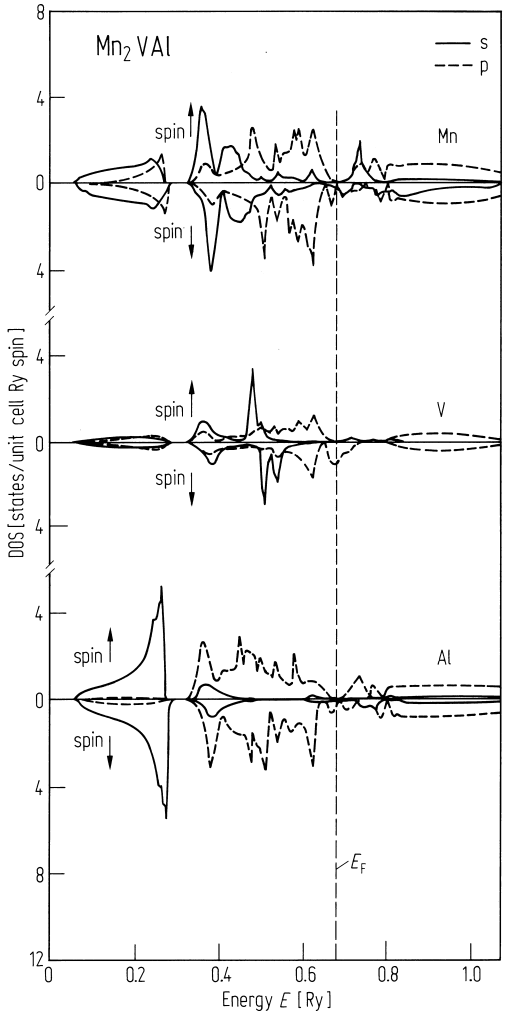

Fig. 445. DOS curves of the s and p states Mn, V and Al in Mn_2VAl calculated using the LSD method [84I2].

X_2YZ X = 4d ; Y = 3d

X = 8A: Ru, Rh
Y = 7A: Mn; 8A: Fe, Ni
Z = 3B: In; 4B: Si, Ge, Sn, Pb

The hyperfine fields have been investigated using Mössbauer ^{119}Sn, ^{57}Fe and ^{111}Cd spectroscopy.

Table 96. Mössbauer results for some Rh_2MnZ and Co_2MnZ alloys [84D1].

	T = 77 K		T = 295 K	
	$\overline{H}$ [kOe]	IS [mms^{-1}]	$\overline{H}$ [kOe]	IS [mms^{-1}]
$Rh_2MnGe_{0.98}Sn_{0.02}$	– 48 ± 1	1.43 ± 0.02	– 42 ± 1	1.41 ± 0.02
Rh_2MnSn	31 ± 1	1.46 ± 0.02	18 ± 1	1.40 ± 0.02
$Co_2MnGe_{0.98}Sn_{0.02}$	6.5 ± 0.5	1.54 ± 0.02		
Co_2MnSn	102 ± 3	1.55 ± 0.02		

Table 95. A summary of the hyperfine fields, isomer shifts and half-widths of the Mössbauer lines for some Rh-based Heusler alloys [86J1].

		H_{hf} on ^{119}Sn			H_{hf} on ^{121}Sb
		T = 4.2 K	T = 77 K	T = 293 K	T = 77 K
Rh_2MnGe	H [kOe]	(–) 46.1(4)	(–) 45.7(5)	– 39.0(4)	
	IS [mm s^{-1}]	– 1.1(1)	– 1.0(1)	– 1.1(1)	
	Γ [mm s^{-1}]	1.7(2)	1.5(2)	1.5(1)	
Rh_2MnIn	H [kOe]		4.86(4), 19.7(2), 35.8(4)	0	
	IS [mm s^{-1}]		– 1.05(1), 1.17(1), – 1.05(1)	– 0.93(1)	
	Γ [mm s^{-1}]		0.92(1), 0.90(1), 1.12(1)	0.91(1)	
Rh_2MnSn	H [kOe]	+ 26.4(3)	+ 26.1(3)	+ 16.5(2)	
	IS [mm s^{-1}]	– 1.1(1)	– 1.1(1)	– 1.1(1)	
	Γ [mm s^{-1}]	1.2(1)	1.2(1)	1.1(1)	
Rh_2MnSb	H [kOe]		18.3(2), (–) 43.6(4), 66.5(6)	– 25.7(3)	(+) 42(4)
	IS [mm s^{-1}]		– 1.08(1), – 1.0(1), – 1.4(1)	– 1.9(2)	– 6.5(2)
	Γ [mm s^{-1}]		1.97(2), 0,94(1), 2.1(2)	1.33(1)	3.7(2)
Rh_2MnPb	H [kOe]	+ 23.4(2)	+ 23.9(2)	+ 8.5	
	IS [mm s^{-1}]	– 1.1(1)	– 1.0(1)	– 1.2(1)	
	Γ [mm s^{-1}]	1.9(2)	2.2(2)	2.2(2)	

Table 97. Magnetic and structural properties of some X_2MnZ alloys [84D1].

Alloy	T_C [K]	a [Å]	p_Z [μ_B]	p_{Mn} [μ_B]	p_{total} [μ_B]	n_0 [Å^{-3}]
Rh_2MnGe	450	6.027			4.62	0.106
Rh_2MnSn	412	6.252			3.10	0.070
Co_2MnGe	905	5.745	0.75	3.61	5.11	0.133
Co_2MnSn	829	6.000	0.75	3.58	5.08	0.116

Table 98. Hyperfine field H_{hf} in kOe at ^{57}Fe and ^{119}Sn dilute impurities which replace Ge in Ru_2FeGe and Rh_2FeGe [83P1] and for comparison Rh_2FeSn [80G1].

	^{57}Fe	^{119}Sn	
	B	D	A, C
Ru_2FeGe	317(3) [1])	90(2) [2])	61(5) [2])
Rh_2FeGe	344(3) [1])	15(3) [2])	
Ru_2FeSn	314(2) [2])	118(2) [2])	84(5) [2])
Rh_2FeSn	296(2) [2])	59(2) [2])	

[1]) At 15 K.
[2]) At 85 K.

Table 99. A summary of the lattice parameters and magnetic data of Ru_2FeSn, Ru_2FeGe, Rh_2FeSn and RhFeGe [83P1].

Alloy	a [Å]	c/a	T_C [K]	p [μ_B/f.u.]
Ru_2FeGe	5.982	1.000	609	1.92 [1])
Rh_2FeGe	5.764	1.074	490	2.19 [1])
Ru_2FeSn	6.200	1.000	593	3.30 [2])
Rh_2FeSn	5.850	1.180	583	3.70 [3])

[1]) In 3 kOe at 77 K.
[2]) In 7 kOe at 77 K.
[3]) In 66 kOe at 4 K.

Table 100. A summary of hyperfine field H_{hf} and related properties in Rh_2MnZ compounds with Z = Ge, Sn and Pb [85J1].

Host alloy	a [Å]	T_C [K]	p_{eff} [μ_B]	k_F [Å^{-1}]	H_{hf} (0K) [kOe]	
					^{111}Cd	^{119}Sn
Rh_2MnGe	6.030(5)	450	4.62	1.47	– 198(3)	– 47(2)
Rh_2MnSn	6.252(5)	412	3.10	1.28	– 141(1)	32(2)
Rh_2MnPb	6.332(5)	338	4.12	1.36	– 144(2)	25(2)

Table 101. Summary of the magnetic and structural properties of Ru-based Heusler alloys [85M3].

Alloy	a [Å]	T_m [K]	p [μ_B/f.u.]	H_{hf} (Fe) [kOe]
Ru_2FeSn	6.20	595 (F)	3.30	314
Ru_2FeGe	5.98	610 (F)	1.92	317
Ru_2FeSi	5.87	280 (AF)	0.04	225

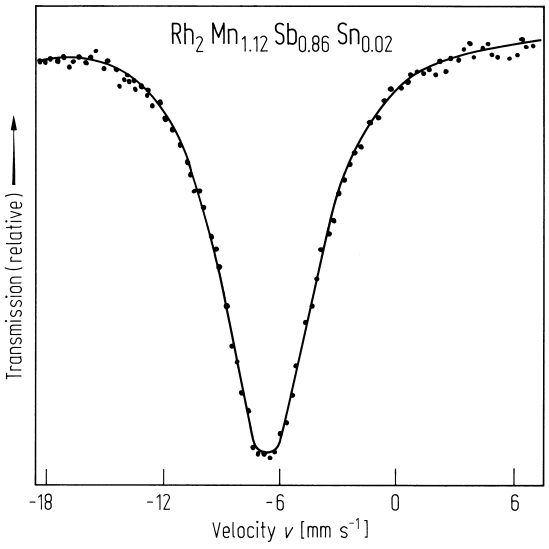

Fig. 447. ^{121}Sb Mössbauer spectrum of $Rh_2Mn_{1.12}Sb_{0.86}Sn_{0.02}$ at 77 K. A least squares fit to the data is shown by a solid line. The natural linewidth of the source was 2.1 mm s^{-1} [86J1].

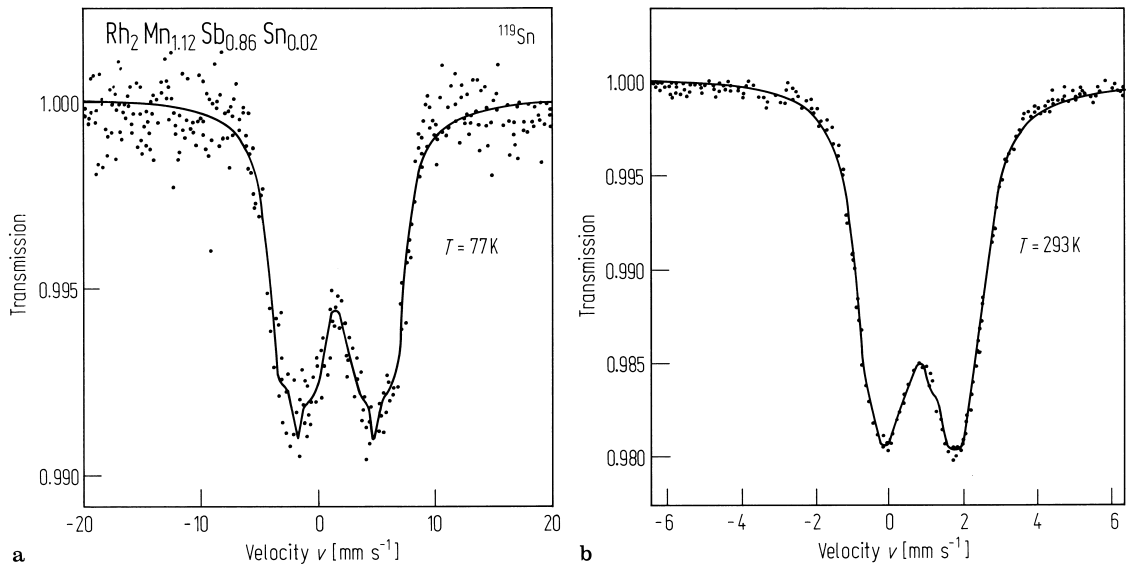

Fig. 446. ^{119}Sn Mössbauer spectrum of $Rh_2Mn_{1.12}Sb_{0.86}Sn_{0.02}$ at (**a**) 77 K and (**b**) 293 K [86J1].

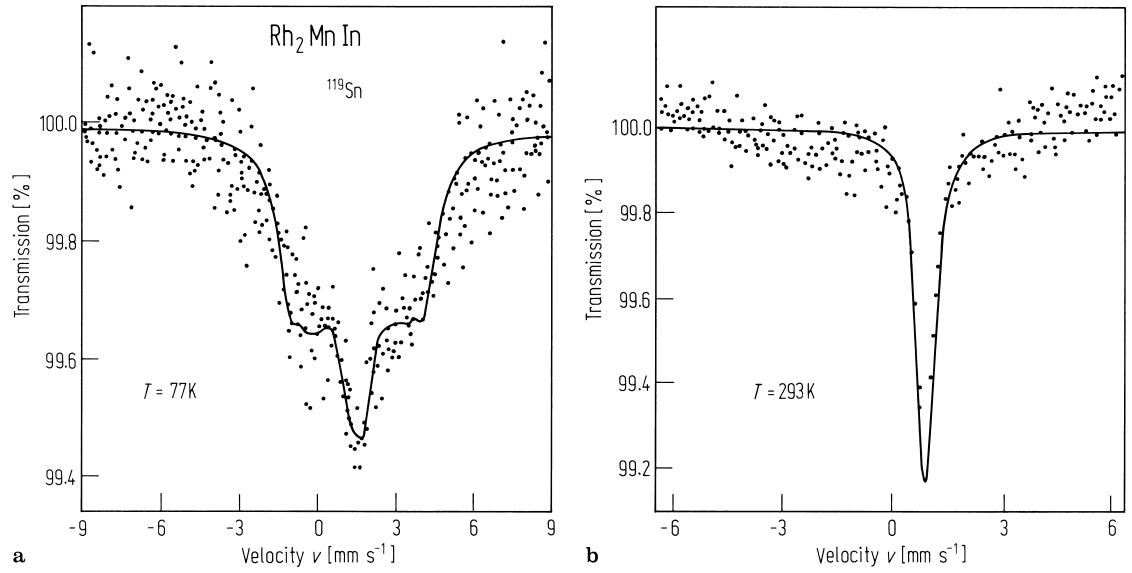

Fig. 448. ^{119}Sn Mössbauer spectrum in Rh_2MnIn at (**a**) 77 and (**b**) 293 K. Computer fits to the data are shown by the solid lines [85J1].

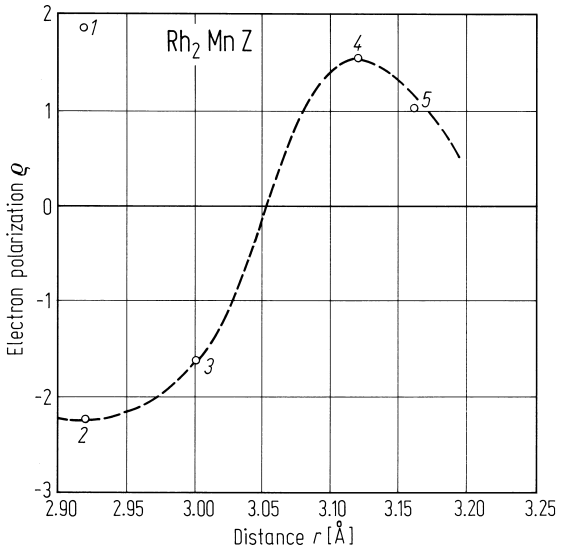

Fig. 449. $\rho(r)$ at ^{119}Sn against r in $Rh_2Mn_{1.12}Sb_{0.88}$ (*2*), Rh_2MnGe (*3*), Rh_2MnSn (*4*), Rh_2MnPb (*5*) and at ^{121}Sb in $Rh_2Mn_{1.12}Sb_{0.88}$ (*1*) [86J1].

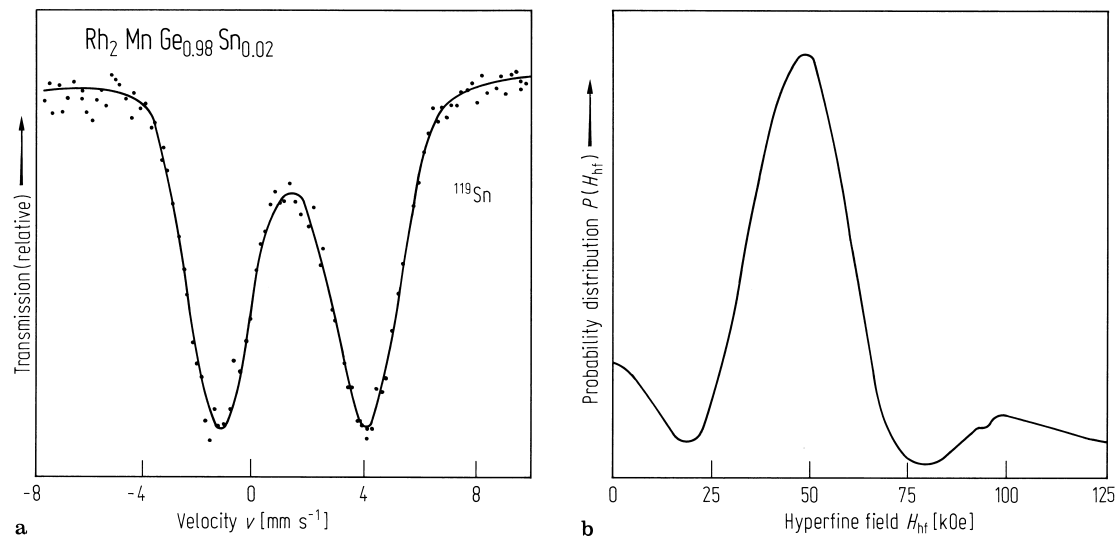

Fig. 450. (**a**) ^{119}Sn Mössbauer effect spectrum of $Rh_2MnGe_{0.98}Sn_{0.02}$ at 77 K and (**b**) hyperfine field probability distribution [84D1].

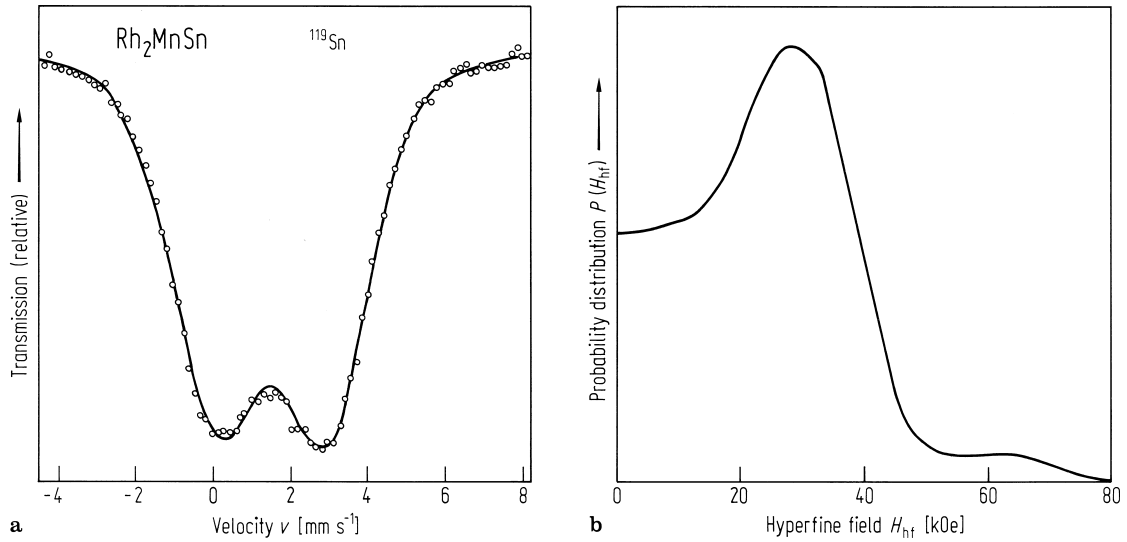

Fig. 451. (**a**) ^{119}Sn Mössbauer spectrum of Rh_2MnSn at 77 K and (**b**) hyperfine field probability distribution [84D1].

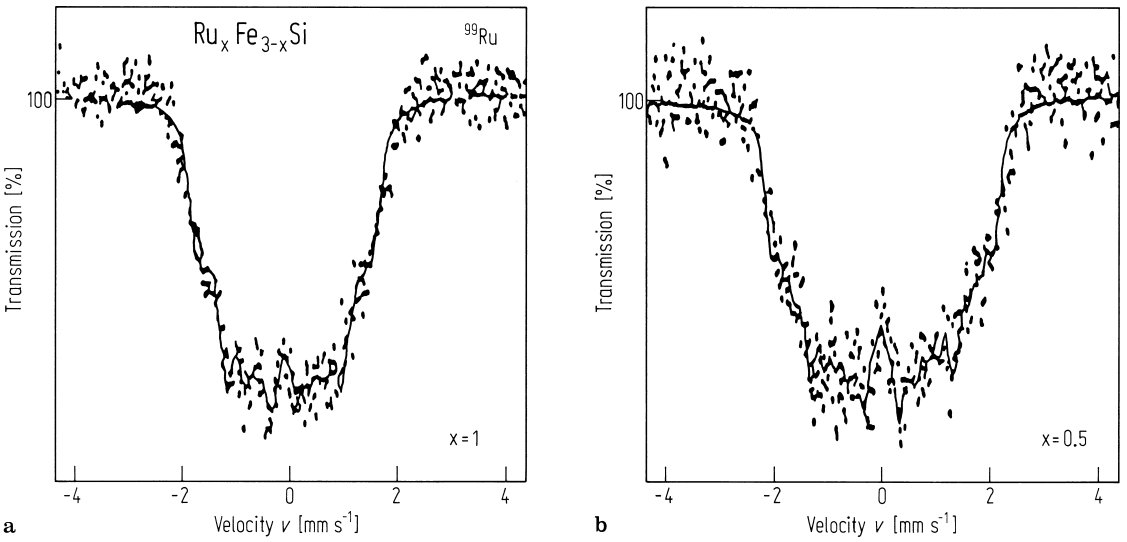

Fig. 452. ^{99}Ru Mössbauer spectra of $Ru_xFe_{3-x}Si$ for (**a**) x = 1 and (**b**) x = 0.5 at 5 K against a ^{99}Rh-Ru metal source at the same temperature [90K2].

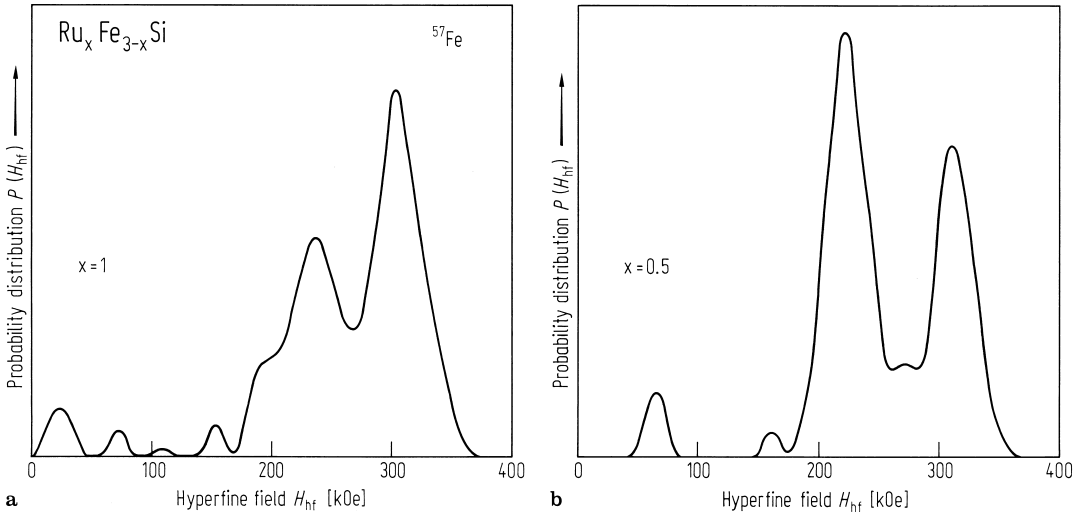

Fig. 453. Hyperfine magnetic field distribution at ^{57}Fe nuclei of $Ru_xFe_{3-x}Si$ (x = 0.5, 1) at 77 K [90K2].

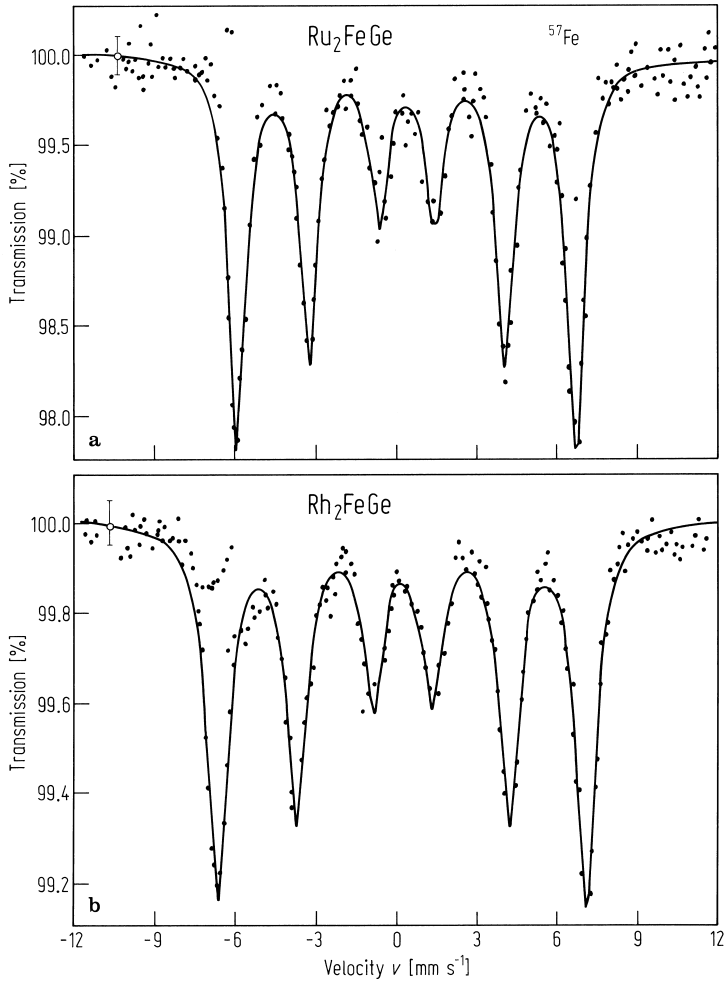

Fig. 455. ^{57}Fe Mössbauer spectra of (**a**) Ru_2FeGe and (**b**) Rh_2FeGe absorbers at 15 K against ^{57}Co(Rh) source [83P1].

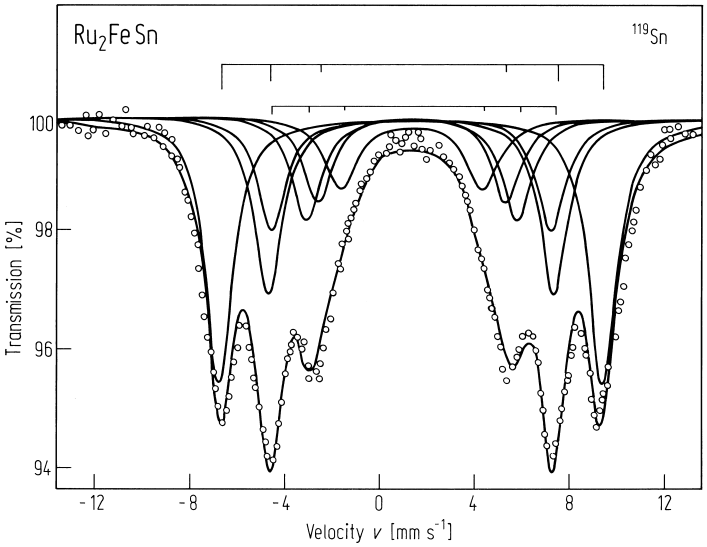

Fig. 454. ^{119}Sn Mössbauer spectrum of Ru_2FeSn at 5 K [90K2].

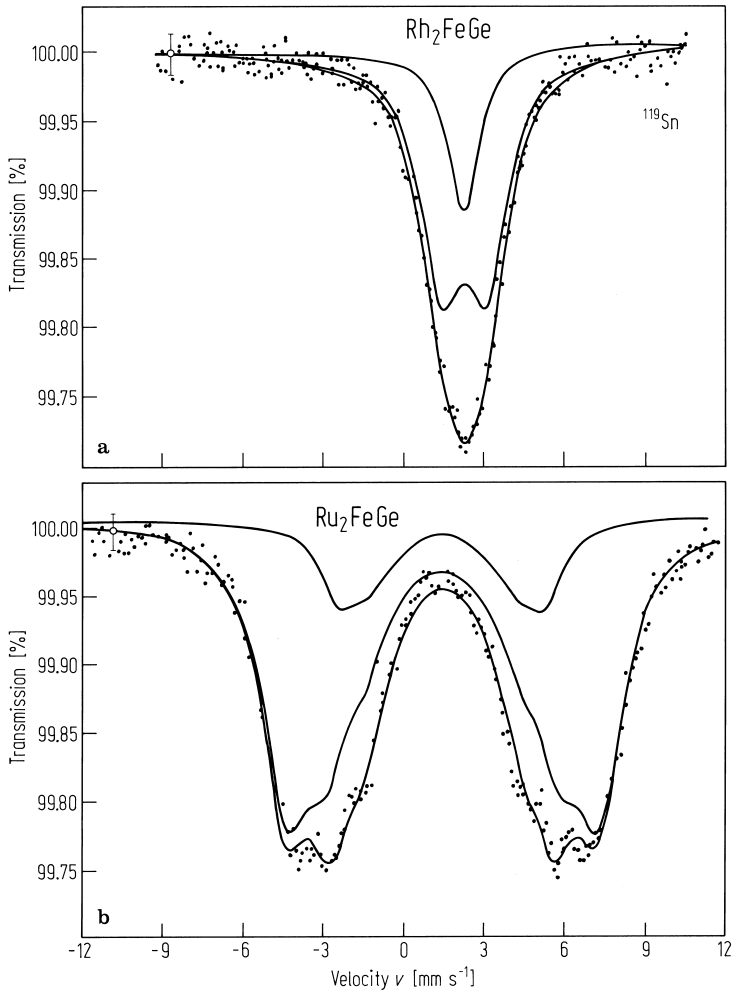

Fig. 456. Mössbauer spectra of ^{119}Sn as a dilute impurity replacing Ge (**a**) Rh_2FeGe and (**b**) Ru_2FeGe absorbers at 85 K against $Co^{119}SnO_3$ source [83P1].

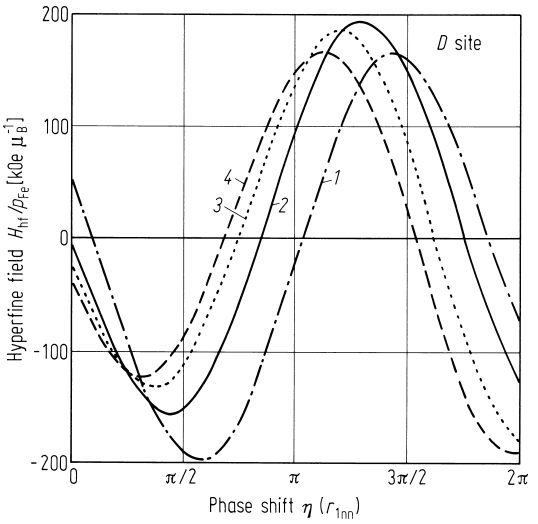

Fig. 457. Reduced hyperfine field at Sn plotted against phase shift for different average valence (*1*) 0.5, (*2*) 0.75, (*3*) 1 and (*4*) 1.25 electrons for atom [83P1]. η: phase shift of conduction electrons.

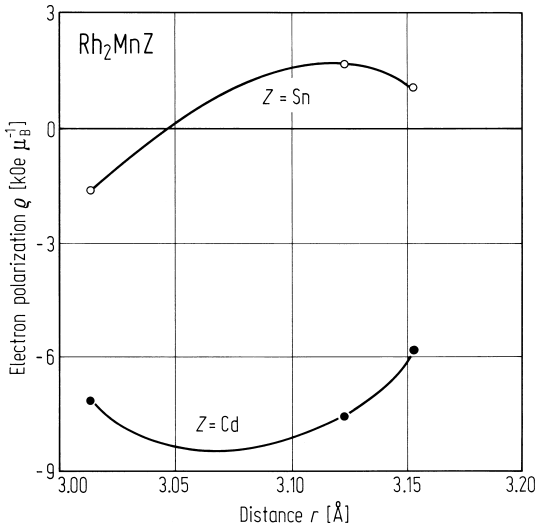

Fig. 460. Conduction electron polarisation for Sn and Cd as a function of the Mn-Z distance in Rh_2MnZ [85J1].

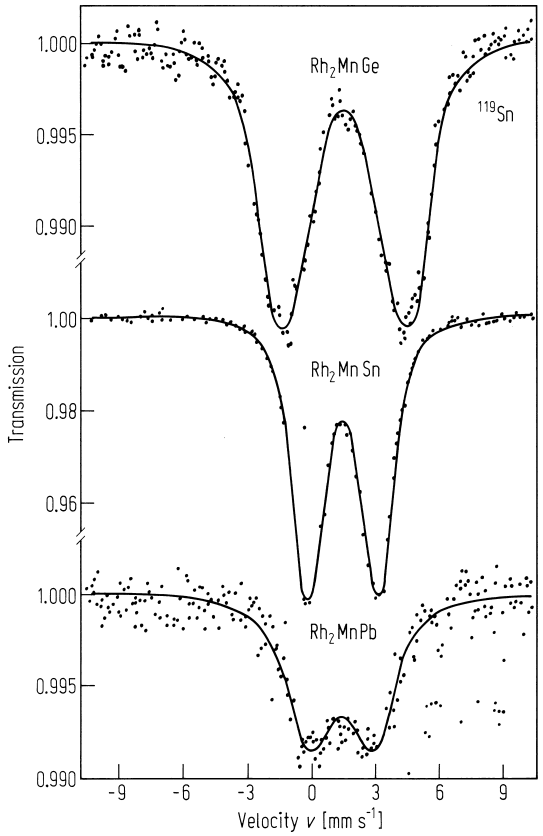

Fig. 459. Mössbauer spectra at 4.2 K for ^{119}Sn in Rh_2MnGe Rh_2MnSn and Rh_2MnPb [85J1].

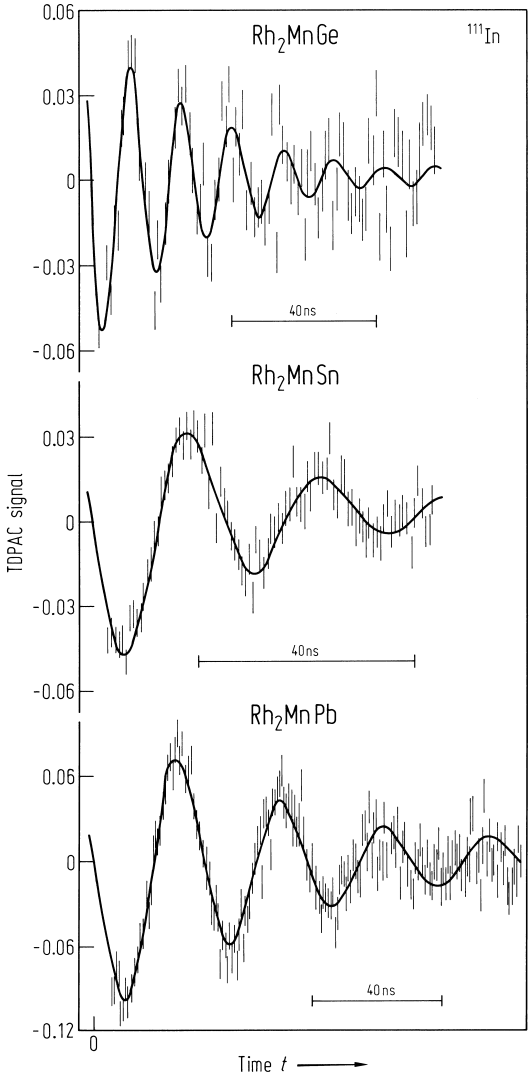

Fig. 458. Room temperature differential perturbed angular correlation (TDPAC) measurements in an external field of 0.6 T for ^{111}In in Rh_2MnGe, Rh_2MnSn and Rh_2MnPb [85J1].

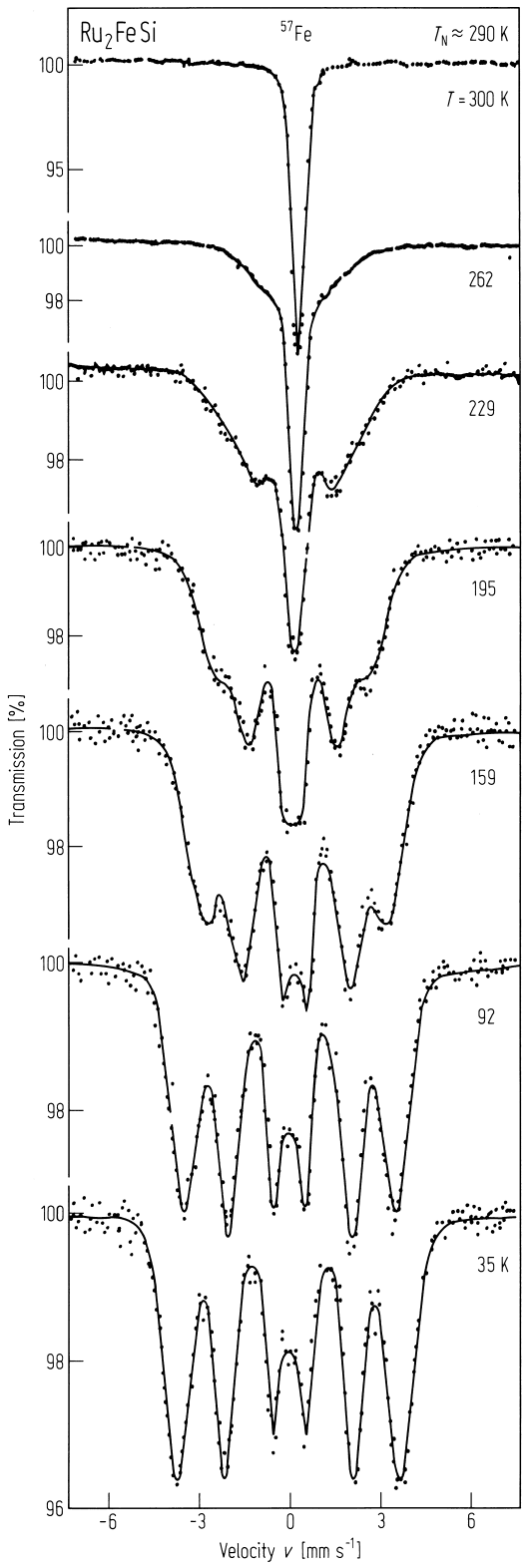

Fig. 461. Mössbauer spectra for Ru_2FeSi are various temperatures obtained using a ^{57}Co(Rh) source. The solid lines are a fit to the data incorporating a field distribution [85M3].

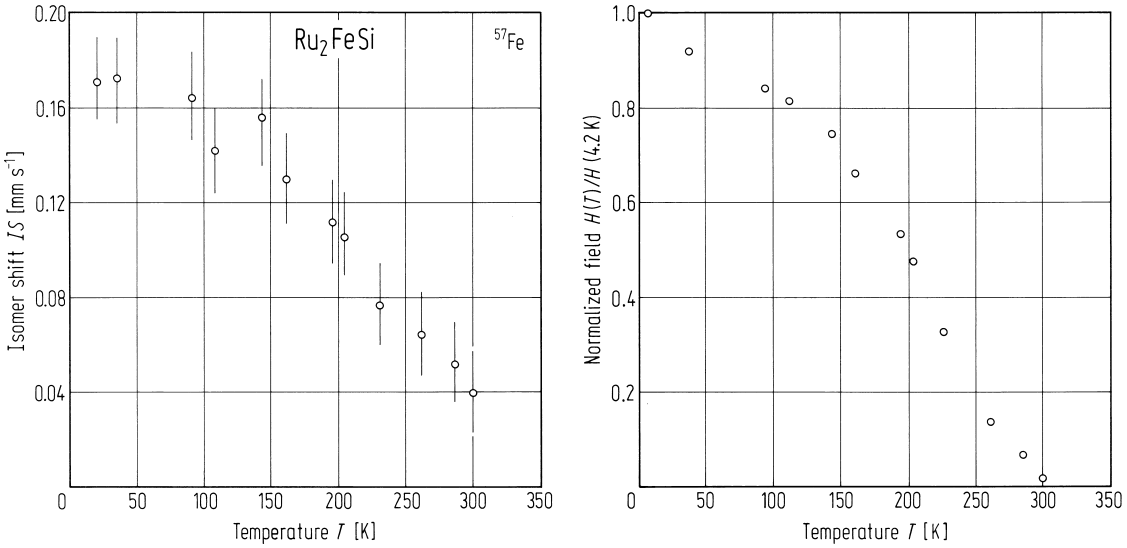

Fig. 462. Average hyperfine field values normalised to 4.2 K and the isomer shift with respect to a ^{57}Co(Rh) source for Ru_2FeSi at various temperatures [85M3].

X_2YZ X = 5d; Y = 3d

X = 8A: Ir
Y = 7A: Mn
Z = 3B: Ga

Ir_2MnGa

The compound orders antiferromagnetically below 65 K. The nuclear spin lattice relaxation time Γ_q of ^{69}Ga and ^{71}Ga has been measured in the paramagnetic state and is consistent with an exchange coupled local moment system.

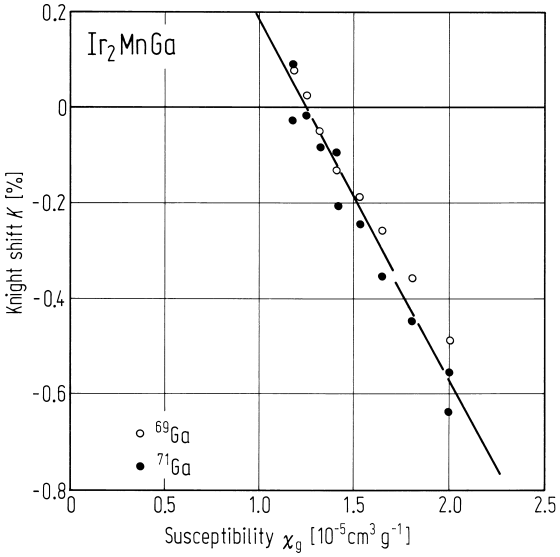

Fig. 465. Plots of the Knight shift (K) vs. susceptibility for ^{69}Ga and ^{71}Ga in Ir_2MnGa [88Y1].

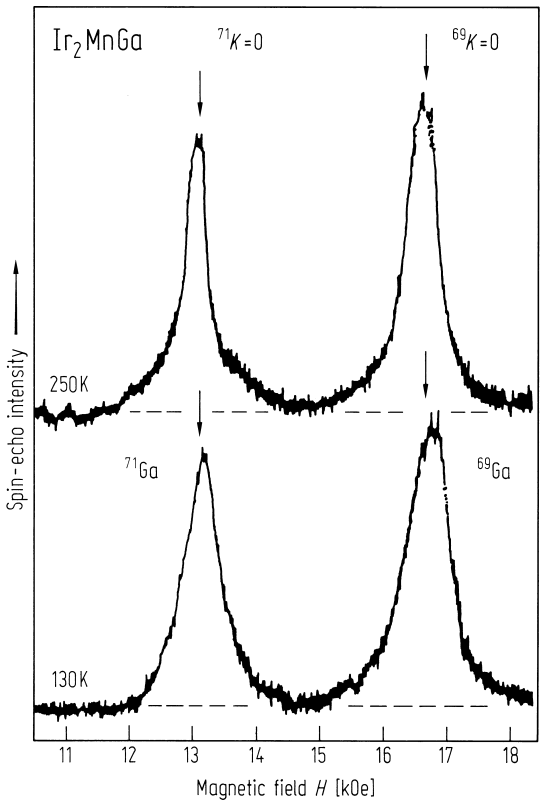

Fig. 463. NMR spectra of ^{69}Ga and ^{71}Ga in Ir_2MnGa [88Y1].

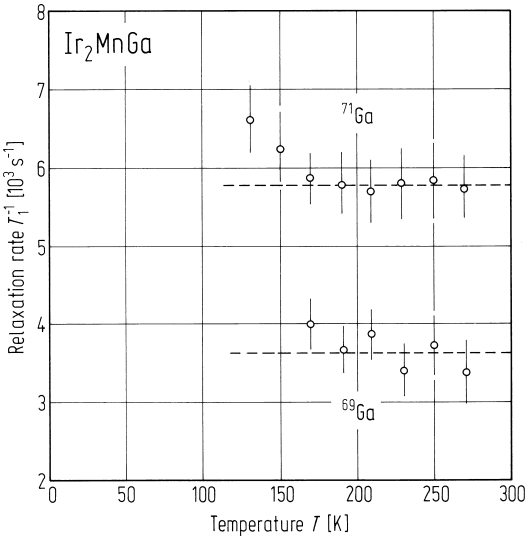

Fig. 466. Temperature dependence of the reciprocal of the relaxation time T_1^{-1} for ^{69}Ga and ^{71}Ga in the paramagnetic state of Ir_2MnGa. The dashed lines represent calculated values. ν = 17.00005 MHz [88Y1].

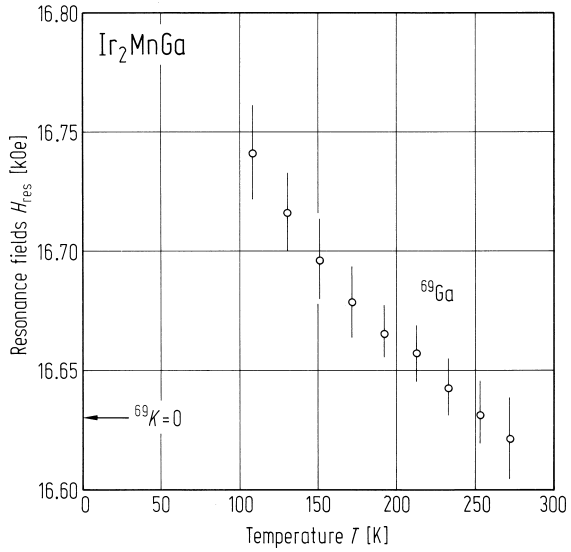

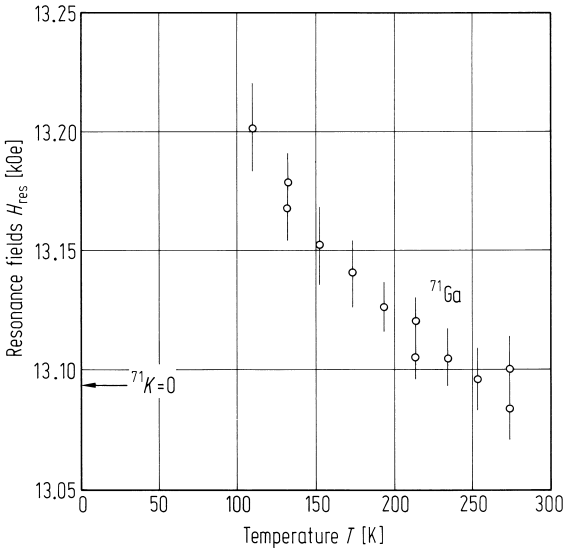

Fig. 464. Temperature dependence of the resonance fields H_{res} for ^{69}Ga and ^{71}Ga in the paramagnetic state of Ir_2MnGa. The arrows show the fields for a zero Knight shift. ν = 17.00005 MHz [88Y1].